Journal of Statistical Physics, Vol. 121, Nos. 5/6, December 2005 (© 2005)
DOI: 10.1007/s10955-005-8665-7

Plants and Fibonacci

Alan C. Newell[1] **and Patrick D. Shipman**[2]

Received December 27, 2004; accepted June 15, 2005

The universality of many features of plant patterns and phyllotaxis has mystified and intrigued natural scientists for at least four hundred years. It is remarkable that, to date, there is no widely accepted theory to explain the observations. We hope that the ideas explained below lead towards increased understanding.

KEY WORDS: Pattern formation; phyllotaxis.

1. INTRODUCTION

Since the time of Johannes Kepler, natural scientists have been fascinated and intrigued by the observation that the phylla (elements such as leaves, florets, stickers or bracts) on many plants are arranged in such a manner that each phyllo lies on three familes of spirals. Moreover, the numbers of arms in each of the spiral families are, in almost 95% of all cases, sequential triads in the regular Fibonacci sequence $1, 1, 2, 3, 5, 8, \ldots$ (Fig. 2(a)). Further, the surfaces of these plants are tiled in polygonal shapes. The challenge is to provide a rational basis for understanding plant patterns, including an explanation for the presence of Fibonacci sequences.

By *plant patterns* we mean both the arrangement of phylla on plants (phyllotaxis) and the tiling of the plant surface into polygonal shapes such as ridges, hexagons, or parallelograms; see Fig. 1. In recent work,(15,16) we have suggested that much of what is observed can be explained by minimizing the elastic energy of a curved annular region of the plant's tunica (outer skin) in the neighborhood of the shoot apical meristem (SAM). In this paper, we seek to address in more depth the question as to the extent

---

[1] Department of Mathematics, University of Arizona, Tucson, AZ 85721; e-mail: anewell@math.arizona.edu
[2] Max Planck Institut für Mathematik in den Naturwissenschaften, Inselstrasse 22, D-04103 Leipzig, Germany; e-mail: shipman@mis.mpg.de

0022-4715/05/1200-0937/0 © 2005 Springer Science+Business Media, Inc.

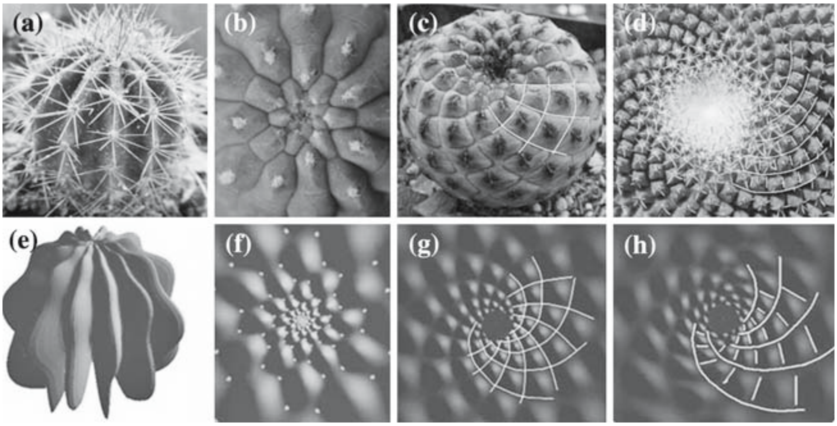

Fig. 1. Common planforms on plants are (a) ridges, (b) irregular hexagons, (c) parallelograms, and (d) staircase parallelograms. Theoretical reproductions of each planform based on the mechanical model presented in Section 4 are shown in (e)–(h). Reprinted from *Journal of Theoretical Biology*, P. D. Shipman and A. C. Newell, Polygonal Planforms and Phyllotaxis, accepted for publication 2005, with permission from Elsevier.

that our results depend on the specific model we postulate rather than on its universal features (e.g., symmetries) which are shared by many descriptions, including the Douady–Couder paradigm explained below. This is important because patterns arising from very different microscopic backgrounds often show very similar features.

Common to all theories of phyllotaxis is that phylla form as small bumps called primordia in a *generative region* near the plant tip. The primordia develop further into, for example, leaves or florets (phylla), and, in the reference frame of the summit of the plant shoot, they move away from the plant tip as the plant grows in height, changing in radial, but not angular coordinate. Thus, if one labels phylla according to their distance from the plant tip, as in Fig. 2(a,c), the nth-numbered phyllo was formed after the $(n+1)$st-numbered phyllo. To understand the formation of plant patterns we thus have several questions to answer, including (i) Can the same theory describe ridge-shaped and polygonal planforms? (ii) In the case of polygonal planforms, what determines the positions at which primordia (the polygons) form near the plant tip and therefore the phyllotactic pattern that develops? and (iii) What determines the type of phyllo that a primordium will develop into?

As plants are biological, and therefore very complex systems, the answers to these questions involve a variety of physical mechanisms interacting at different space and time scales. However, it has been proposed by Douady and Couder$^{(2,3)}$ that phyllotaxis is a very robust phenomenon

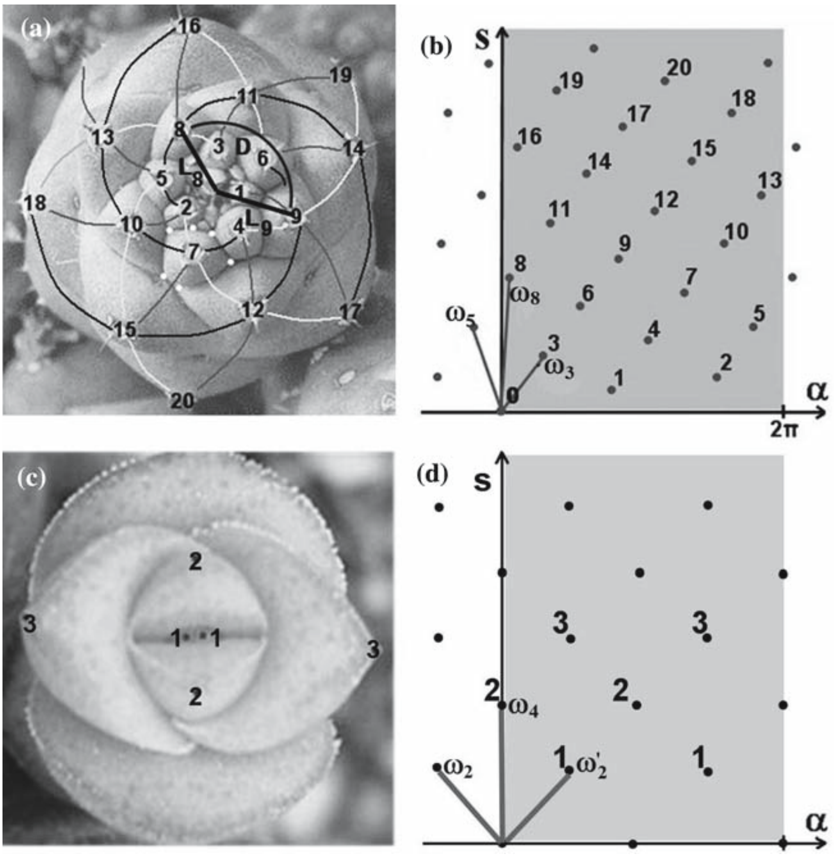

Fig. 2. The phylla of a cactus (a) and a succulent (c) are numbered according to their distance from the center. In (a), lines are drawn connecting neighboring phylla; this produces families of 3 (in black) and 8 (in grey) sets of clockwise spirals and a family of 5 (in white) counterclockwise spirals. (b,d) Putting radial r and angular α coordinates on the plant tip and defining $s = r$ or $s = \ln(r)$, depending on if the plant exhibits the plastochrone difference or ratio (see text), the numbered points form lattices in the (s, α)-plane. The vectors ω_j are natural choices as generating vectors for the lattices. Reprinted from *Journal of Theoretical Biology*, P. D. Shipman and A. C. Newell, Polygonal Planforms and Phyllotaxis, accepted for publication 2005, with permission from Elsevier.

and that many, if not most, of what is observed can be explained by a simple set of dynamical rules formulated by Hofmeister$^{(13)}$ or Snow and Snow$^{(17)}$–that is, the answer to question (ii) is independent of the physical mechanism responsible for producing primordia as long as the mechanism satisfies a few basic criteria. The central idea of Hofmeister, set out in Section 3, is that each new primordium should be placed in the most "open" space available to optimize its ability to grow into fully matured phylla. Douady and Couder constructed an experimental paradigm for these rules in which a set of repelling points (which represent primordia) are introduced at fixed time intervals at the center of a plate.

Our picture is radically different. We do not suggest that individual primordia are formed to optimize their own individual growth progress, but rather that the pattern that forms is a global one and that plant surfaces in the generative region are, to a good approximation, linear combinations $\sum_{j=1}^{N} a_j \cos(l_j r + m_j \alpha)$ of elementary periodic deformations, i.e., modes $\cos(l_j r + m_j \alpha)$, where r and α are respectively radial and angular coordinates centered at the summit of the plant tip. The choices of wavevectors $\vec{k}_j = (l_j, m_j)$ and real amplitudes a_j are determined by the physical mechanism and minimize, in our physical model, the elastic energy of a curved, elastic annulus (the generative region) under mechanical stresses (due to growth). We suggest that, while some general features of the phyllotactic pattern can be captured by members of a general class of models sharing Hofmeister and/or Snow or Snow rules, there are other features which are only captured by specific properties of the elastic sheet model. Further, we note that the interplay between stresses in the plant's tunica, changes in the microstructure of the biological material and growth hormones (e.g., auxin), which play crucial roles in the later development of fully mature phylla, is important, but for the first approximation our picture suggests that the deformed surface is produced by purely mechanical means. This model follows the pioneering work of Paul Green and his colleagues at Stanford who argued, in the 1990's, that various growth processes lead to compressive stresses in the plant's tunica in an annular zone near its shoot apical meristem. In a series of papers, they gave detailed reasons and provided experimental evidence to support this picture.(9–12,18) What they did not recognize was how crucial the quadratic nonlinear interactions of the linearly most unstable modes are in the competition for dominance. These interactions lead naturally to most, if not all, of the phyllotactic patterns observed. They arise from that part of the in-place strain energy which is the product of the perturbed Airy stress and the Gaussian curvature of the deformed surface, and the key observation is that this energy is minimized by special triads of modes whose wavevectors satisfy the condition $\vec{k}_1 + \vec{k}_2 = \vec{k}_3$. By "special triads" we mean that the preferred wavevectors are those that maximize a combination of their linear growth rates $\sigma(\vec{k}_j)$ and an interaction coefficient $\tau(\vec{k}_1, \vec{k}_2, \vec{k}_3 = \vec{k}_1 + \vec{k}_2)$. Both σ and τ contain specific information regarding the physical mechanism.

Our goal in this short paper is to use comparisons with the Douady–Couder paradigm and the results of their energy functional based on mutually repelling primordia in order to argue in favor of the Green model which starts from premises which are well supported by experiment. The description of phyllotaxis in terms of phyllotaxis coordinates is presented in Section 2. In Section 3 we delineate the premises and give the main results of the DC model. We write the premises of our biomechanical model in a parallel format in Section 4.1. In Section 4.2, we discuss the growth ($\sigma(l, m)$) and interaction (τ) coefficients and show that, as the plant grows, the energy-minimizing configuration evolves due to combinations of a new, most linearly unstable circumferential mode and the influence of already formed configurations which have moved out of the generative region. In Section 5, we discuss how the key difference of our model from the DC paradigm—that the mechanical model leads to a study of the interaction of elementary modes and the calculation of their amplitudes, whereas the Douady–Couder paradigm assumes the interaction of primordia—allows us to address both questions (i) and (ii) and has potential consequences for question (iii).

2. PHYLLOTACTIC PARAMETERS

In this section, we find the natural coordinates in which to state the position of phylla on a plant and thus to describe phyllotaxis. In Fig. 2(a,c), phylla are numbered according to their distance from the centers of the plants. This allows us to illustrate the following three standard parameters used to describe phyllotactic patterns:

1. The whorl number g: Each phyllo on a plant is a member of a whorl of g phylla that are evenly spaced about a circle centered at the center of the plant. The number g is locally constant. For the example of Fig. 2(c), $g = 2$, as one sees pairs of phylla that are equidistant from the center of the plant. For the cactus of Fig. 2(a), $g = 1$.

2. The divergence angle $D = 2\pi d$: The angle between consecutively numbered phylla is taken to be the angle between the rays from the center of the plant to the centers of those phylla; see Fig. 2(a). It is an observation that the angle between any two consecutively numbered phylla is locally constant on any plant; this constant is called the *divergence angle*, $D = 2\pi d$. There is a natural ambiguity in the measurement of the angle, as one can either measure clockwise or counterclockwise. If the two measurements are not equal, the plant shows a *handedness* and $D = 2\pi d$ is taken to be the smaller of the two measurements; thus, $0 < d \leqslant \frac{1}{2}$. In our Fig. 2(a) example, the divergence angle is roughly $D = 2\pi(0.382)$ measured clockwise, and for the example of Fig. 2(c), $D = \frac{2\pi}{4}$ measured either counterclockwise or clockwise.

3. The plastochrone ratio λ: Call the length of the ray from the center of the plant to the center of the nth-numbered phyllo L_n; see Fig. 2(b). The standard claim of the phyllotactic literature is that on most plants, at least for phylla close the center, the ratio $\frac{L_{n+1}}{L_n}$ is locally independent of n. That ratio is called the *plastochrone ratio*. It seems that on many cacti it is the difference $L_{n+1}-L_n$ that is constant. For such plants that difference we shall call the *plastochrone difference*. We will denote this parameter by λ.

The observations leading to parameters g, d and λ tell us that the arrangement of phylla on plants is a lattice. To see this pictorially, put radial and angular coordinates (r, α) on the cactus of Fig. 2 and then transfer the result to Fig. 2(b), where dots represent the centers of phylla, and the vertical axis is $s=\log(r)$ if the plant exhibits the plastochrone ratio and $s=r$ if the plant exhibits the plastochrone difference. We choose the direction of increasing α to be the direction determined by the clockwise or counterclockwise handedness. If the plant has whorl number g, divergence angle $D=2\pi d$ and plastochrone ratio λ, in the (s, α)-plane the plant's phylla are part of a lattice $\Omega(\vec{\omega}_{\lambda,d}, \vec{\omega}_g)$ that is the integer span of the vectors $\vec{\omega}_{\lambda,d}=(\lambda, 2\pi d)$ and $\vec{\omega}_g=(0, \frac{2\pi}{g})$ where λ equals $\log(\lambda)$ or λ if λ is a plastochrone ratio or difference, respectively. The bases of $\Omega(\vec{\omega}_{\lambda,d}, \vec{\omega}_g)$ are exactly the linear combinations

$$\begin{aligned} \alpha\vec{\omega}_{\lambda,d}+\beta\vec{\omega}_g &= \left(\alpha\lambda, 2\pi(d\alpha+\tfrac{\beta}{g})\right)=\tfrac{1}{g}(g\alpha\lambda, 2\pi(g\alpha d+\beta)), \\ \gamma\vec{\omega}_{\lambda,d}+\delta\vec{\omega}_g &= \left(\gamma\lambda, 2\pi(d\gamma+\tfrac{\delta}{g})\right)=\tfrac{1}{g}(g\gamma\lambda, 2\pi(g\gamma d+\delta)), \end{aligned} \tag{1}$$

where α, β, γ, and δ are integers such that $\alpha\delta-\beta\gamma=\pm 1$. Setting $m \doteq g\alpha$, $n \doteq g\gamma$, $p \doteq \delta$, $q \doteq \beta$, we have that all of the bases of the lattice $\Omega(\vec{\omega}_{\lambda,d}, \vec{\omega}_g)$ are given by

$$\begin{aligned} \vec{\omega}_m &= \tfrac{1}{g}(m\lambda, 2\pi(md-q)), \\ \vec{\omega}_n &= \tfrac{1}{g}(n\lambda, 2\pi(nd-p)), \end{aligned} \tag{2}$$

where m, n, p, q are any integers such that $pm-qn=\pm g=\pm$ gcd(m,n); gcd(m,n) means the greatest common divisor of m and n. Often there is a natural choice of the integers m and n to describe a phyllotactic pattern. For example, in Fig. 2.1(a), the choice $m=3$ and $n=5$ corresponds to the families of 3(5) spirals proceeding clockwise (counterclockwise) from the center of the plant; the vectors ω_3 and ω_5 as marked in Fig. 2.1(b) then form a natural basis for the phyllotactic lattice. The choice for m, n used to describe the pattern is referred to as the *parastichy pair*. The choice of parastichy pair used to describe a pattern has some degree of ambiguity; for example, the eight clockwise spirals of Fig. 2.1(a) justify a possible choice of $(5, 8)$. For lattices with $g > 1$, spirals are not as easily traced out by the eye. We will take the convention of stating the choice $(m, n) = (g, g)$ as the parastichy pair for such a pattern; the corresponding lattice generators (2) are marked as ω_2 and ω_2' in Fig. 2.1(d).

It is observed in plants that the Fibonacci sequence arises as the parastichy pair of a phyllotactic pattern undergoes transitions, starting with lower numbers such as $(m, n) = (1, 2)$ or $(m, n) = (2, 3)$ and moving up the sequence $1, 2, 3, 5, 8, \ldots$ (i.e., $(1, 2) \to (2, 3) \to (3, 5) \to \cdots$), typically as the plant grows in width. These transitions arise in both our model and that of DC as continuous (second order, Type II) transitions. Transitions in which the parastichy pair moves up the sequence $(2, 2) \to (2, 3) \to (3, 3) \to \cdots$ are also observed in nature and arise as discontinuous (first order, Type I) transitions in the models.

3. HYPOTHESES OF HOFMEISTER AND THE SNOWS, AND THE DOUADY–COUDER PARADIGM

Phylla are only formed near the tip of a plant, so that the phyllotactic patterns as seen in Fig. 2 are the result of a prolonged process in which phylla form and then move away from the plant tip as the shoot grows in height. This process is described by three of five rules formulated by Wilhelm Hofmeister in 1868. As stated by Douady and Couder,(12) these rules are

1. The stem apex (Fig. 3) is axisymmetric.

2. The primordia are formed at the periphery of the apex (Region 2 in Fig. 3) and, due to the shoot's growth, they move away from the center with a radial velocity $V(r)$ which may depend on their radial location.

The next two Hofmeister rules concern the determination of the positions at which the primordia form, i.e. the choice of divergence angle $2\pi d$. These will be stated in the next section. The last Hofmeister rule reads

5. Outside of a region of radius R (Region 3 of Fig. 3), there is no further reorganization leading to changes in the angular position of the primordium.

Our discussion now will focus on what belongs in slots 3. and 4.–what determines if and where primordia are formed in the generative region.

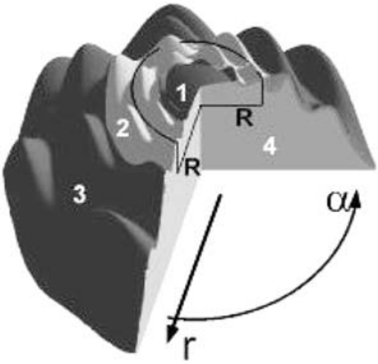

Fig. 3. Schematic representation of the shoot apical meristem (SAM). The SAM consists of a thin skin (the *tunica*, Regions 1,2,3 in the diagram) attached to a foundation of less well organized cells (the *corpus*, Region 4 in the diagram). Cells in Region 1 show little growth activity and Region 2 is the *generative region* in which active cell division is occuring and new primordia are first seen to form. As the plant tip grows, cells move from Region 2 to Region 3, radially outward in the reference frame of the diagram's north pole. In Region 3, primordia that formed in Region 2 further develop into mature elements such as leaves. In Section 4, radial r and angular α coordinates on the tunica surface in the generative region are defined by projecting the surface to the polar coordinates on the plane. Reprinted from *Journal of Theoretical Biology*, P. D. Shipman and A. C. Newell, Polygonal Planforms and Phyllotaxis, accepted for publication 2005, with permission from Elsevier.

Concerning positions at which primorida form in the generative region, Hofmeister proposed the rules

3. New primordia are formed at regular time intervals (the plastochrone T).
4. The incipient primordium forms in the largest space available left by the previous ones.

Douady and Couder (DC) sought the simplest experiment that could simulate the Hofmeister rules. Their basic experimental device is a plate with a small central dome in the mddle; this is to represent to the plant with the apex at the tip. The plate is placed in a vertical magnetic field that is stronger at the edges of the plate than in the middle, and ferromagnetic drops (representing primordia) are periodically dropped onto the center of the central dome (representing the apex). The drops fall to the perimeter of the central dome and then move radially outward, following the gradient of increasing magnetic strength. The magnetic field is chosen so that the velocity $V(r)$ in an exponentially increasing function of the radius. After choosing a radial direction in which to fall from the top of the central dome, the drops do not change their angular coordinate. How the drops initially choose their angular coordinate is of interest, and here the central point is that the drops form repelling magnetic dipoles. A drop that falls on the central dome moves to the position on the boundary of the dome as determined by the repulsions of the drops that recently formed and are moving away from the center, and the experimental result is that a there is constant divergence angle between the angular coordinates of successively-dropped drops. Denoting the radius of the central dome by R, the initial speed of the drops after falling to the boundary of the dome by V_0, and the time period in which drops are dropped onto the central dome by T, the plastochrone ratio of the resulting pattern is $G \doteq \frac{V_0 T}{R}$. G is a parameter chosen by the experimenter. As Douady and Couder decrease G, the divergence angle between succesive drops approaches the golden angle and a lattice pattern with a Fibonacci parastichy pair is produced.

As the Hofmeister rules (3) and (4) and the electromagnetic paradigm assume that one primordium forms at a time, the Hofmeister rules do not allow for the formation of whorl patterns with $g > 1$ as in Fig. 2(c). DC thus turned to a revised set of hypotheses of Snow and Snow;(17) as stated by Douady and Couder,(4) the revised rules read

3. The apex is in the shape of a parabaloid, and the primordia can have an azimuthally elongated shape.
4. A new primordium forms when and where a large enough space has been formed at the periphery of the apex.

The area of a primordium and the growth of the primordia and apex now play central roles. DC imagine primordia as circles with diameter d_0 on a parabaloid with curvature described by a parameter N. For $N = 1$, the apex is flat, and for $N > 1$, the apex has curvature. Projected to the plane, the circular primordia on a curved apex will be elongated in the angular direction, so $N > 1$ can be thought of as describing azimuthally (angularly) elongated primordia. As a primordium of diameter d_0 occupies space that can then not be taken by another primordium, DC imagine that each primordium generates a repulsive energy $E(d)$, where d is the distance from the primordium. Projecting the apex parabaloid onto the plane and using polar coordinates, DC employ the distance function

$$d(P_0, P_1) = \sqrt{\left[\frac{r_0^2 - r_1^2}{N} + 2Nr_0r_1\left(1 - \cos(\theta_0 - \theta_1)\right)\right]}. \qquad (3)$$

between two points with coordinates $P_0=(r_0,\theta_0)$ and $P_1=(r_1,\theta_1)$, and the repulsive energy that a primordium exerts on points a distance d from it is given by

$$E(d)=\frac{-1+\left(\tanh\alpha\frac{d}{d_0}\right)^{-1}}{-1+(\tanh\alpha)^{-1}}. \tag{4}$$

Here α is a "stiffness" parameter; for lower α, a primordium has a larger influence on other points. Thus, any point on the generative circle of radius R from the apex summit has a repulsive energy exerted on it by each of the previously formed primordia that have since moved radially outward. The energy $E(\theta)$ of a point $P=(R,\theta)$ on the generative circle is defined to be the sum of the repulsive energies exerted on that point by each of the previously formed primordia. As the primordia move outward, the energy $E(\theta)$ decreases at any point. DC show that it is equivalent to say that a space of diameter d_0 (and therefore a potential spot for a new primordium to form on the generative radius) has formed as it is to say that the energy $E(\theta)$ becomes lower than some threshold value at that point. Thus, to simulate the Snow and Snow hypothesis 4., DC allow a primordium to form on the generative circle where and whenever $E(\theta)$ decreases to the threshold value. In numerical experiments, DC investigate the phyllotactic patterns that form as the parameter $\tilde{\Gamma}=\frac{d_0}{R}$ decreases. They employed two schemes. In the first scheme, starting from a large value of $\tilde{\Gamma}$, they let n consecutive particles appear, where n was large enough to allow for a steady-state regime to appear and varied from up to 150 to 500. Then, starting from the positions of the last approximately 20 deposited primordia, they decreased $\tilde{\Gamma}$ a small amount and let particles form again until a steady-state regime was found. For the second scheme, DC began with a few primordia having a configuration that was expected to be either stable or unstable and observed whether or not the pattern continued to grow.

The main geometric parameter that determines the pattern that develops is the ratio $\tilde{\Gamma}$, which plays a role analogous to that of G in the electromechanical paradigm. Both whorled and spiral phyllotactic arrangements of primordia were produced in the numerical experiments, with larger parastichy numbers for smaller values of $\tilde{\Gamma}$, and to simulate a typical plant, DC sought to understand what happens as $\tilde{\Gamma}$ decreases from a large value.

1. For large values of $\tilde{\Gamma}$, the relative stability of the whorled and spiral modes is determined by the conicity N and stiffness α parameters. The decussate (alternating 2-whorl) (2,2,4) configuration could only be

obtained for large values of the conicity parameter N. The exploration of various values of α showed that large values of α (i.e., short-range interactions) favor whorled modes, whereas small values favor spiral modes. Thus, in the DC model, the whorled decussate mode $(2, 2)$ can only exist at large $\tilde{\Gamma}$ with either azimuthally elongated primordia or with conical apices and short-range interaction.
2. As $\tilde{\Gamma}$ is decreased, Type I transitions in which the parastichy numbers increase up the sequence $(n-1, n) \rightarrow (n, n) \rightarrow (n, n+1) \rightarrow \cdots$ are observed. However, the transition between, for example, a (1,2,(3)) spiral state and a (2,2,(4)) decussate state is not abrupt; in between there is a transitory state in which the divergence angle varies periodically.
3. For low $\tilde{\Gamma}$, Type I transitions to whorled modes of higher order continue to occur. To produce Type II transitions and therefore spiral patterns, DC take $\tilde{\Gamma}(t)$ as a rapid function of time. The system then does not have enough time at a given value of $\tilde{\Gamma}$ to make a transition to a whorled mode, and a continuous change $(m, n) \rightarrow (n, m+n)$ to the next spiral mode occurs.

The DC model is thus able to capture both whorled and spiral phyllotaxis, with transitions between patterns determined by the evolution of $\tilde{\Gamma}$. The suggestion of DC is that any microscopic mechanism must contain the simple dynamial rules of their model in that it (1). defines finite-sized primordia and (2). allows for an interaction (repulsion or attraction) of the primordia.

By assuming that primordia of a given shape form, the Douady–Couder paradigm focuses on the phyllotactic question (ii). In the case of polygonal planforms, what determines the positions at which primordia (the polygons) form near the plant tip and therefore the phyllotactic pattern that develops? Thus, the formation of ridges and various polygonal configurations such as hexagons and parallelograms are not captured by their model.

4. BIOMECHANICAL MODEL

4.1. Justification for and Hypotheses of a Biomechanical Model

Our goal now is to formulate a biomechanical model for the formation of plant patterns. Green, *et al.* have provided the following evidence that a biomechanical mechanism underlies the plant pattern formation:

1. Hernández and Green(12) grew a sunflower head between two fixed parallel bars. This resulted in an amplification of undulations parallel to the bars, and phyllotaxis followed this pattern. This external mechanical influence also changed the identity of the sunflower bracts.

2. Green(9) induced a new row of leaves to form on an expanding meristem by using a glass frame to apply a mechanical constraint.
3. Steele(18) noted that the turgor pressure inside plant cells is between 7 and 10 atmospheres, and that this large pressure can hardly be ignored in the phyllotactic process. Also, in this paper, Steele notes a linear relationship between the size of primordia and the thickness of the tunica.
4. In,(5) Dumais and Steele showed sunflowers cut along a diameter. The two sides of the cut stick together only in the region of the surface where the pattern formation is occurring, indicating that the compressive force keeping the cut closed is related to the pattern formation.
5. Fleming *et al.*(7) were able to induce primordia on tomato plants by locally applying the protein expansin; some of these primordia then developed into leaf-like structures. The known effect of the extracellular expansin proteins is to increase cell wall extensibility, thus changing the mechanical properties of the plant material.

In the review article(9) Green outlines the hypothesis that buckling of the compressed tunica is the main mechanism determining phyllotactic pattern. Green continues to discuss evidence for feedback mechanisms between the buckling configuration and changes in cellulose orientation in cell walls and direction in cell division; buckling is thus only one component in the complex process of building the pattern, and it is interesting to note that similar feedback mechanisms between changes in stresses and changes in cellulose orientation have been noted for wood cells in tree branches.(6,19) However, the hypothesis of Green is that the reasons for Fibonacci patterns and the difference between Types I and II transitions can be found within the buckling mechanism.

The first three hypotheses of our model are modeled on the first three hypotheses of Snow and Snow as stated by DC. They read

1. The stem is axisymmetric.
2. A normal deflection w of the generative region at the periphery of the apex is produced and advected out in the reference frame of the apex summit.
3. The curvature of the annular generative region can be described by signed radii of curvature R_α and R_r in the angular and radial directions, with R_j taken to be positive if the surface along the j coordinate line bends away from the normal vector (see Fig. 4). In this article, we assume that $R_\alpha = R_r$ so that the curvature of the generative region is as pictured in either Fig. 4 (a) or (b), depending on the sign of R_α. More general shapes are included in,(16) but are not essential for our argument. The coordinates r and α are placed on the annular generative region by projection to the polar coordinates on the plane; see Fig. 4.

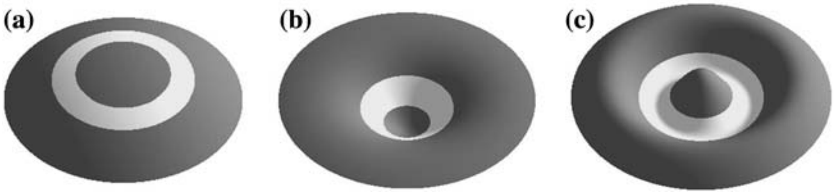

Fig. 4. (a) Spherical ($R_\alpha, R_r > 0$), (b) Inverted Spherical ($R_\alpha, R_r < 0$), and (c) Hyperbolic ($R_\alpha > 0$, $R_r < 0$) geometries of the generative region, denoted by light shading. Reprinted from *Journal of Theoretical Biology*, P. D. Shipman and A. C. Newell, Polygonal Planforms and Phyllotaxis, accepted for publication 2005, with permission from Elsevier.

The key difference from the statement of the rules by DC is that we consider a deformation w of the generative region instead of assuming the formation of primordia. The next two hypotheses are specific to the mechanism of mechanical buckling in the generative region as the source of pattern formation.

4. The generative region of the plant apex is modeled as a thin, elastic spheroidal shell (the tunica, Region 2 in Fig. 2.2) attached to an elastic foundation (the squishy corpus, Region 4 in Fig. 2.2) and under compressive stresses due to growth. The growth stresses develop if either the tunica is growing faster than the corpus foundation or, in the case $R_\alpha < 0$, if the corpus foundation is growing faster than the tunica. We assume that the compressed tunica shell will buckle to minimize the elastic energy of the shell-corpus, thus giving the deformation w. Thus, in this first model, we are ignoring possible plastic or viscoelastic properties of the plant material.
5. Outside of a region of radius R, the deformation w may grow in amplitude (*i.e.*, $w \mapsto \eta w$, $\eta > 1$), but there is otherwise no change in the pattern.

The main task of our analysis is the find the elastic energy-minimizing deformation w of the tunica in the generative region. In the Föppl-von Kármán–Donnell (FvKD) theory,$^{(1,8)}$ the elastic energy of the thin tunica shell can be written as a functional of the normal deflection w of the tunica shell and the Airy stress function f, which is a potential for the in-plane stresses; indeed, assuming that the stresses are constant through the width h of the tunica shell, and denoting the stress tensor by σ_{ij},

$$f_{rr} = h\sigma_{\alpha\alpha}, \quad f_{r\alpha} = -h\sigma_{r\alpha}, \quad f_{\alpha\alpha} = h\sigma_{rr}.$$

We write in (5) below the dimensionless energy, where the dimensionless parameters are written in terms of the natural buckling wavelength, namely the length of the most linearly unstable mode. The natural wavelength is given by $2\pi\Lambda$, where

$$\Lambda^4 = \frac{Eh^3\nu^2}{\kappa + \frac{Eh}{R_\alpha^2}},$$

for Young's modulus E, Poisson's ratio ν and the Hooke's constant κ of the elastic foundation. Two parameters in the energy express the geometry of the generative region and two give the stress tensor.

The first geometric parameter is the ratio

$$\Gamma = \frac{R}{\Lambda}$$

of the circumfrance $2\pi R$ of the central circle in the generative region to the natural wavelength $2\pi\Lambda$; this is roughly the inverse of the DC parameter $\tilde{\Gamma}$ and will play an analogous role in our model. Approximating the Laplacian by the Euclidean Laplacian $\Delta = \partial_r^2 + \frac{1}{\Gamma^2}\partial_\alpha^2$ (instead of the Laplacian $\partial_r^2 + \frac{1}{\Gamma}\partial_r + \frac{1}{\Gamma}\partial_\alpha^2$ we simplify the analysis; notice that this simplification is similar to that used by DC in that it is valid if pattern formation is determined by what happens on the circle of radius R. Assuming that the two radii of curvature in the generative region are of equal magnitude (so the apex is spherical; more general shapes are discussed in ref. 18), the second geometric parameter expresses the dimensionless curvature

$$C = \frac{\Lambda^2}{R_\alpha h\nu}$$

of the apex *in the generative region*. This is analogous to the DC conicity parameter N, *but* notice that, whereas C is strictly relevant at radius R from the apex summit where new primordia are forming, the parameter N expresses the conicity of the entire apex and is essential for determing the effect of old primordia on newly formed primordia.

Experimental evidence indicates that the largest compressive stress in the generative region is along the angular coordinate line;(5) the principle stresses (averaged through the width of the shell) are thus $N_{rr} = h\sigma_{rr}$ and $N_{\alpha\alpha} = h\sigma_{\alpha\alpha}$. The corresponding dimensionless parameters are

$$P = -\frac{N_{\alpha\alpha}\Lambda^2}{Eh^3\nu^2}, \qquad \chi = \frac{N_{rr}}{N_{\alpha\alpha}}.$$

Scaling the radial coordinate by $2\pi\Lambda$, the dimensionless elastic energy functional is given by

$$\mathfrak{E}(w,f)=\int\left[\begin{array}{ll}\frac{1}{2}(\Delta w)^2+V(w) & -\frac{1}{2}P\left(\chi\partial_r w+\frac{1}{\Gamma^2}\partial_\alpha w\right)^2 \\ & +f\left(C\Delta w-\frac{1}{2\nu\Gamma^2}[w,w]\right) \quad -\frac{1}{2}(\Delta f)^2\end{array}\right]dr\ d\alpha, \tag{5}$$

where $[f,w]=f_{rr}w_{\alpha\alpha}+f_{\alpha\alpha}w_{rr}-2f_{r\alpha}w_{r\alpha}$, and consists of the following terms: The first term in (5) resists buckling and corresponds to the bending energy of the shell. $V(w)$ is a potential coming from the elastic foundation and an applied pressure from corpus growth; we take $V(w)=\frac{\kappa}{2}w^2+\frac{\gamma}{4}w^4$ for spring constants κ and γ. The next two terms are a strain energy, approximately equal to the Airy stress function multiplied by the Gaussian curvature.(7) The final term arises from in-surface deformations. The dimensionless FvKD equations for an overdamped shell are the variational equations $\zeta w_t=-\frac{\delta\mathfrak{E}}{\delta w}$, $0=-\frac{\delta\mathfrak{E}}{\delta f}$, so that, after scaling t,

$$\begin{aligned}&w_t+\Delta^2 w+\kappa w+\gamma w^3+P\left(\chi\partial_r^2 w+\frac{1}{\Gamma^2}\partial_\alpha^2 w\right)+C\Delta f-\frac{1}{\nu\Gamma^2}[f,w]=0,\\&\Delta^2 f-C\Delta w+\frac{1}{2\nu\Gamma^2}[w,w]=0.\end{aligned}\tag{6}$$

The first equation is the stress equilibrium equation, and the second gives a compatibility condition relating w and f. Note that the parameter Γ can be hidden in the equations by scaling $\alpha\mapsto\frac{1}{\Gamma}\alpha$.

When the stress P is larger than some critical value P_c, the uniform static solution $w_0=0$, $f_0=-P(\chi r^2+\alpha^2)$ of the FvKD equations is linearly unstable and certain shapes and configurations are preferentially amplified. We write the deviations $w(r,\alpha,t)$ from w_0 as $\sum_{j=1}^{N}(A_j(t)\mathrm{e}^{\mathrm{i}l_j r+\mathrm{i}m_j\alpha}+$ complex conjugate) and the deviations $f(r,\alpha,t)$ from f_0 in terms of the $A_j(t)$ by solving iteratively the compatibility equation $0=\frac{\delta\mathfrak{E}}{\delta f}$. Substituting these expressions into (5) and averaging over space, the perturbation energy $\mathfrak{E}(w,f)$ becomes

$$\begin{aligned}\mathfrak{E}=&-\sum_{\vec{k}\in\mathfrak{A}}\sigma_j(l_j,m_j)A_jA_j^*-\sum\tau_{123}\left(A_1A_2A_3+A_1^*A_2^*A_3^*\right)\\&+\sum_{c,d=1}^{N}\gamma_{cd}A_cA_c^*A_dA_d^*.\end{aligned}\tag{7}$$

Details of the calculation are given in.(16) The first sum in (7) is taken over all wavevectors which are in the *active set* $\mathfrak{A}$, which is the set of $\vec{k}_j$ for which the (real) linear growth rates $\sigma(l_j, m_j)$ are greater than some small negative number (to allow for subcritical bifurcations). The cubic terms in (7) arise from all wavevector triads in $\mathfrak{A}$–that is, all triplets $\vec{k}_1, \vec{k}_2, \vec{k}_3$ of wavevectors in $\mathfrak{A}$ such that $\vec{k}_1 + \vec{k}_2 = \vec{k}_3$. The coefficient $\tau_{123}(\vec{k}_1, \vec{k}_2, \vec{k}_3 = \vec{k}_1 + \vec{k}_2)$, given below, is a function of the triad wavevectors. The quartic terms are positive definite and are mainly due to the elastic foundation (the squishy corpus). As the system is overdamped, the time dependence of the $A_j(t)$ are given by gradient flows $\zeta \frac{\partial}{\partial t} A_j = -\frac{\delta \mathfrak{E}}{\delta A_j^*}$, and therefore $\{A_j(t)\}_1^N$ relax to local minima in $\mathfrak{E}$. Our task is to find energy-minimizing configurations.

As the energy-minimizing amplitudes A_j are found to be real numbers, the energy-minimizing deformation $w(r, \alpha) = \sum_{j=1}^{N} (A_j(t) \mathrm{e}^{\mathrm{i} l_j r + \mathrm{i} m_j \alpha} +$ complex conjugate) can be written as $w(r, \alpha) = \sum a_j \cos(\vec{k}_j \cdot \vec{x})$, $a_j = 2A_j$, $\vec{x} = (r, \alpha)$. This energy-minimizing $w(r, \alpha)$ is the theoretical calculation for the buckling pattern in the generative region. Assuming that the pattern formed in the generative region remains the same as material moves radially outward from the generative region (our hypotheses 2. and 5.), after the tip has grown a length r_g, the observed pattern is given by the graph of the function $w(s, \alpha)$, $0 < s < r_s$, where $s = r, r_s = r_g$ or $s = \ln(r)$, $r_s = \ln(r_g)$, depending on if the radial growth is constant or exponential. This leads in the former case to a pattern with the plastochrone difference, and in the latter case to one with the plastochrone ratio.

It will convenient for the analysis in Section 4 to connect the deformation $w(r, \alpha)$ with the phyllotactic lattice generators 2 in the case when

$$w(r, \alpha) = \sum_{j=1}^{N} a_j \cos(\vec{k}_j \cdot \vec{x}), \tag{8}$$

where the wavevectors $\vec{k}_j$ are integer combinations of two wavevectors $\vec{k}_m = (l_m, m)$ and $\vec{k}_n = (l_n, n)$ (for example, if $w(r, \alpha) = \sum_{j=1}^{3} a_j \cos(\vec{k}_j \cdot \vec{x})$, where $\vec{k}_1 + \vec{k}_2 = \vec{k}_3$). The maxima of the deformation (8), where each wavevector is an integer combination of

$$\vec{k}_m = (l_m, m) = \left(\frac{2\pi}{\lambda}(q - md), m \right), \qquad \vec{k}_n = (l_n, n) = \left(\frac{2\pi}{\lambda}(p - nd), n \right), \tag{9}$$

for given choices of d, λ, m, n and p, q such that $pm - qn = \pm g$, occur on a lattice spanned by the generators of phyllotactic lattices given by (2), namely

$$\vec{\omega}_m = \frac{1}{g}(\lambda m, 2\pi(md - q)), \qquad \vec{\omega}_n = \frac{1}{g}(\lambda n, 2\pi(nd - p)). \tag{10}$$

The relationship between a pair of wavevectors (9) and the dual pair (10) of lattice generators can be expressed by defining the matrices

$$K = \begin{pmatrix} \vec{k}_n \\ \vec{k}_m \end{pmatrix} = \begin{pmatrix} \frac{2\pi}{\lambda}(p - nd) & n \\ \frac{2\pi}{\lambda}(q - md) & m \end{pmatrix}, \quad \Omega = (\vec{\omega}_m, \vec{\omega}_n) = \frac{1}{g}\begin{pmatrix} \lambda m & \lambda n \\ 2\pi(md - q) & 2\pi(nd - p) \end{pmatrix}$$

such that

$$K\Omega = \pm 2\pi I.$$

As the radial coordinate in (5) is scaled by the natural wavelength $2\pi\Lambda$, the modulus $A = 2\pi\frac{\lambda}{g}R\Lambda$ of the determinant of the matrix

$$\Omega' = (\vec{\omega}_m, \vec{\omega}_n) = \frac{1}{g}\begin{pmatrix} \lambda\Lambda m & \lambda\Lambda n \\ 2\pi R(md - q) & 2\pi R(nd - p) \end{pmatrix}$$

approximates the area of a newly formed primordium (ignoring the curvature of the apex in the generative region and assuming that the size of the primordium is small compared to R).

4.2. Energy-Minimizing Configurations

4.2.1. The Most Unstable Mode; Ridge Planforms

The first task in minimizing the energy (7) is to determine the set $\mathfrak{A}$ of active modes and the properties of the coefficient $\sigma(l, m)$. The linear growth of a mode with wavevector $\vec{k} = (l, m)$ is

$$\sigma(l, m) = -\left(l^2 + \frac{1}{\Gamma^2}m^2\right)^2 + P\left(\chi l^2 + \frac{1}{\Gamma^2}m^2\right) - 1. \tag{11}$$

The smallest value of P for which there is a mode with nonnegative linear growth is the *critical value* $P_c = 2$, at which $\sigma(l = 0, m = \Gamma) = 0$. For $P > P_c$, there is a set of modes with positive linear growth rates, but the *critical wavevector* $\vec{k}_c = (0, \Gamma)$ remains the mode with the largest linear growth rate. The derivation of the energy (7) assumes that the stress parameter P is slightly above the critical value P_c, so that, if $\chi = 0$, this set is a small disk centered at $\vec{k}_c = (0, \Gamma)$; see Fig. 5(a). Notice that, for $\chi = 0$, for any fixed angular wavenumber m, the growth rate $\sigma(l, m)$ as a function of l is maximized for $l = 0$.

As the angular wavenumber must be an integer, the most linearly unstable deformation is $w_c = \cos(m\alpha)$ for the closest integer m to Γ. This deformation corresponds to ridge patterns (as seen, for example, on a pumpkin). The energy (7), however, also contains nonlinear terms that allow for the interaction of modes in the active set, so the deformation w_c may (for large enough nonlinear interaction) be unstable to a configuration consisting of a sum of multiple modes. We formally take the set of active modes to be the set of modes with wavevectors $\vec{k}$ such that $\sigma(\vec{k}) > -3\sigma(\vec{k}_c)$; see Fig. 5(a). Practically, we find the set of modes that minimizes the energy (7), and the growth rates for these sets of modes will have positive or slightly negative growth rates.

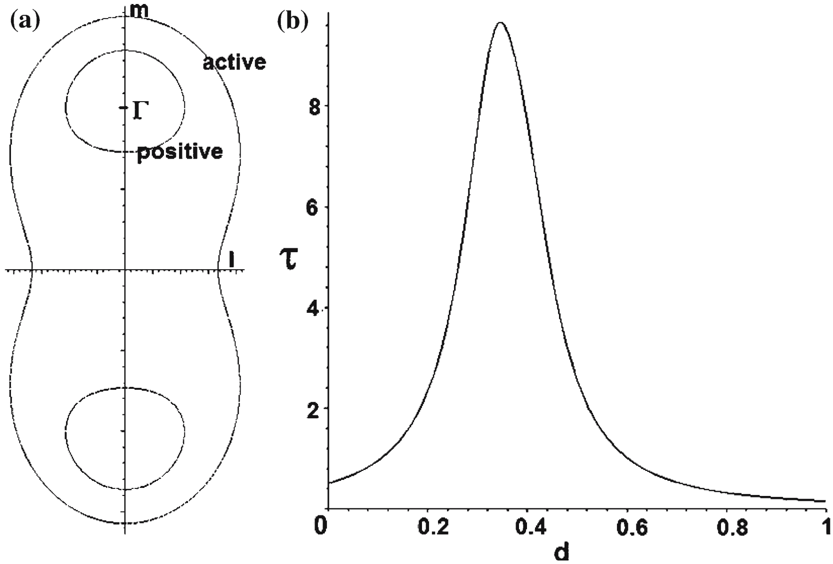

Fig. 5. The coefficients σ and τ of the averaged elastic energy. (a) The positive and active modes for the elliptic shell with $\chi = 0$ and $P = 2.4$. (b) The coefficient $\tau(\lambda, d, n, m, m+n)$ as a function of d for the choices $\frac{C}{\nu} = -3, \Gamma = 8, m = 3, n = 5, \lambda = 1.5$.

4.2.2. The Most Unstable Triad; Hexagon Planforms

As the key nonlinear interaction is encoded in the cubic coefficient

$$\tau(\vec{k}_r, \vec{k}_s, \vec{k}_{r+s} = \vec{k}_r + \vec{k}_s) = \tau(r, s, r+s) = -\frac{C}{\nu\Gamma^2}(l_r m_s - l_s m_r)^2 \times \sum_{j=r,s,r+s} \frac{1}{l_j^2 + \frac{1}{\Gamma^2} m_j^2}, \tag{12}$$

we first describe key characteristics of how τ depends on the parameters and choices of wavevectors.

0. As in σ, the angular wavenumber m and parameter Γ only appear in τ in the ratio $\frac{m}{\Gamma}$. The parameter Γ can be scaled, through m, out of the energy (7).
1. τ is proportional to the curvature constant C; when $C=0$ the quadratic coefficient in the amplitude equations vanishes. This means that ridges are the only stable solutions of the amplitude equations when $C=0$. Note that the appearance of C in the amplitude equations comes from there being nonzero curvature in the original, unbuckled shell. τ is positive for $C<0$ (i.e., for the hyperbolic or inverted spherical generative region, Fig. 4 (b,c)) and negative for $C>0$ (i.e., for the spherical generative region, Fig. 4(a)).
2. As $l_r m_s - l_s m_r = l_r m_{r+s} - l_{r+s} m_r = l_s m_{r+s} - l_{r+s} m_s$, $\tau(\vec{k}_r, \vec{k}_s, \vec{k}_{r+s})$ is a symmetric function of the wavevectors.
3. What values of the radial wavenumbers maximize τ? For a fixed value of m_j, the fraction

   $$\frac{1}{\left(l_j^2 + \frac{1}{\Gamma^2} m_j^2\right)^2}$$

   is maximized for $l_j = 0$. If, however, two radial coordinates are equal to zero, then τ also equals 0 due to the factor $(l_r m_s - l_s m_r)^2$. *For fixed angular wavenumbers, the coefficient τ achieves local maxima at where exactly one of the radial coordinates is zero.*

   Writing the radial wavevectors in terms of the phyllotactic coordinates, $\tau(r, s, r+s)$ becomes

$$\tau = -\frac{C}{\nu}(2\pi)^2 \left[\frac{1}{2\pi\left(\Gamma\frac{q-md}{g}\right)^2 + m^2\frac{\lambda^2}{g^2}} + \frac{1}{2\pi\left(\Gamma\frac{p-nd}{g}\right)^2 + n^2\frac{\lambda^2}{g^2}} + \frac{1}{2\pi\left(\Gamma\frac{p+q-(m+n)d}{g}\right)^2 + (m+n)^2\frac{\lambda^2}{g^2}} \right] \tag{13}$$

From this last expression, we see that the condition that exactly one of the radial coordinates is zero means that $\tau(m,n,m+n)$*, as a function of* d*, achieves local maxima at the three values* $d=\frac{p}{n}, \frac{q}{m}, \frac{p+q}{m+n}$ *that make one of the radial coordinates equal to zero.* In fact, τ is a very sensitive function of d, as illustrated in the graph of τ as a function of d in Fig. 5(b). Also from (13) one sees that *the coefficient* τ *is larger for smaller* λ*–that is, for larger* l_1*,* l_2*.*

4. What values of the angular wavenumbers maximize τ? Writing $\vec{k}_1=(l_1,m_3-m)$, $\vec{k}_2=(l_2,m)$, $\vec{k}_3=(l_1+l_2,m_3)$, fixed m_3 and arbitrary values of C and Γ, τ is maximized at $m=\frac{|l_2|m_3}{|l_1|+|l_2|}$. In particular, we will be interested in the case $l_1=-l_2$, $\vec{k}_3=(0,m_3=\Gamma)$, for which τ is maximized at $\vec{k}_1=(l,\frac{m_3}{2})$, $\vec{k}_2=(-l,\frac{m_3}{2})$.

We first assume for simplicity that $\Gamma=2N$ for some integer N. Then, the most unstable mode as P increases above threshold has wavevector $\vec{k}_c=(0,\Gamma=2N)$. However, for large enough $\tau(\vec{k}_m,\vec{k}_n,\vec{k}_c)$ this ridge solution, with amplitude $A_c=\frac{\sigma(0,2N)}{3\gamma}$, can become unstable to a triad of modes with wavevectors $\vec{k}_m,\vec{k}_n,\vec{k}_c$, where $\vec{k}_m+\vec{k}_n=\vec{k}_c$. The energy (5) allows for multiple triads, but as a first step we seek to find the most unstable single triad configuration. Writing $\vec{k}_m=(l,m)=\frac{1}{g}(\frac{2\pi}{\lambda}(q-md),m)$ and $\vec{k}_n=(-l,n)=\frac{1}{g}(\frac{2\pi}{\lambda}(p-nd),n)$, we need to determine what choices of l m and n (or, equivalently, what choices of λ and d and m,n) and corresponding amplitudes A_m, A_n, A_c give the lowest energy single-triad configuration. The following points in this consideration correspond in numbering to the list of properties for τ.

0. The parameter Γ only affects the chosen triad through a scaling of the angular wavenumbers.
1. As τ is proportional to C, for $C=0$, ridges ($A_c=\frac{\sigma(\vec{k}_c)}{3\gamma}$, $A_m=0=A_n$) are the only solution to the amplitude equations. For larger $|C|$ there are *special* triads for which τ is large enough for there to be a "hexagon" solution with all three amplitudes nonzero. For $C<0$ (the inverted sphere), the amplitudes are all positive, whereas for $C>0$ (the sphere), the amplitudes are all negative.
2. As τ is a symmetric function of the wavevectors, from the inequality $\sigma(\vec{k}_c)>\sigma(\vec{k}_n)$ for all wavevectors $\vec{k}_n$ in $\mathfrak{A}$ follows the amplitude inequality $|A_c|>|A_n|$. We will, in fact, find $|A_c|>|A_m|\simeq|A_n|$, with the ratio $\frac{|A_n|}{|A_c|}$ increasing to 1 as $|C|$ increases.
3. The linear growth rates $\sigma(\vec{k}_m)$ and $\sigma(\vec{k}_n)$ are largest for m,n as close as possible to $\Gamma=2N$ under the constraint $m+n=2N$; also, assuming that $\tau=\tau(\vec{k}_m,\vec{k}_n,\vec{k}_c=(0,2N))$, τ is maximized for the choice $m=n=N$.

Numerical experiments give $m=n=N$ as the energy-minimizing choice of angular wavenumbers.

4. As $\vec{k}_c=(l_c=0,2N)$, we have that $\vec{k}_m=(l,m=N)$, $\vec{k}_n=(-l,n=N)$. There tension between σ and τ as to the best choice of l; σ is maximized for $l=0$, whereas τ is maximized for $l=\infty$. However, the critical wavenumber choice $l_c=0$, i.e., $d=\frac{p+q}{m+n}$, is in the range of large τ even for small choices of l. This allows for there to be a compromise choice, numerically determined to be $l\simeq 1$ for $\chi=0$; larger values of χ give larger values of l, but l remains near 1 for reasonable values of χ.

Hence, for $\Gamma=2N$ and large enough $|C|$, the energy-minimizing triad configuration is $w=\sum_{j=m,n,m+n}A_j\cos(\vec{k}_j\cdot\vec{x})$ with $\vec{k}_m=(l,N), \vec{k}_n=(-l,N)$, and $\vec{k}_{m+n}=\vec{k}_c=(0,2N)$ and with positive (respectively, negative) real A_j for $C<0$ (respectively, $C>0$). For $\Gamma=2N+1$, it is no longer possible to choose $m=n$; in the energy-minimizing configuration, $m=N, n=N+1$. Examples for $\Gamma=12$ and $C<0$ are shown in Fig. 1(a) and, for larger $|C|$, in Fig. 1(b). For $C>0$, the centers of the hexagons would be the minima instead of the maxima of the configuration.

We next address the question of transitions between these configurations as the size of Γ increases. As Γ increases from $2N$ to $2N+1$ and on up, the energy-minimizing triad changes in the sequence

$$\begin{array}{l} \vec{k}_N=(l,N) \\ \vec{k}'_N=(-l,N) \\ \vec{k}_{2N}=(0,2N) \end{array} \rightarrow \begin{array}{l} \vec{k}_N=(l,N) \\ \vec{k}_{N+1}=(-l,N+1) \\ \vec{k}_{2N+1}=(0,2N+1) \end{array} \rightarrow \begin{array}{l} \vec{k}_{N+1}=(l,N+1) \\ \vec{k}_{N+1}=(-l,N+1) \\ \vec{k}_{2N+1}=(0,2(N+1)) \end{array} \rightarrow \cdots . \tag{14}$$

As Γ increases from $2N$ to $2N+1$ and then from $2N+1$ to $2N+2$, there is an abrupt change in the optimal triad, but the triad always has the form $\vec{k}_m=(l,m), \vec{k}_n=(-l,n), \vec{k}_{m+n}=(0,m+n=\Gamma)$, where we find that l does not depend on Γ (l is of order 1 and does depend on χ as discussed above). Writing the wavevectors in the standard form $\vec{k}_m=(l_m=\frac{2\pi}{\lambda}(q-md),m), \vec{k}_n=(l_n=\frac{2\pi}{\lambda}(p-nd),n), \vec{k}_{m+n}=(\frac{2\pi}{\lambda}(p+q-(m+n)d),m+n)$, we see that $\vec{k}_{m+n}=(0,\Gamma)$ implies that $d=\frac{p+q}{m+n}=\frac{p+q}{\Gamma}$, and therefore $l=l_m=-l_n=\pm 2\pi\frac{g}{\lambda}\frac{1}{\Gamma}$. As l is constant with respect to Γ, the ratio $\frac{g}{\lambda}$ changes like Γ. As a consequence, the area $A=2\pi\frac{\lambda}{g}R\Lambda=2\pi\frac{\lambda}{g}\Gamma\Lambda^2=\frac{(2\pi\Lambda)^2}{l}$ of a primordium is constant with respect to Γ.

These are transitions of Type I. As noted in Section 2, these transitions are observed in nature, particularly on plants (e.g., saguaro cacti) for which the configuration is dominated by ridges (i.e., on plants for which $\frac{|A_1|}{|A_3|}$ is small), although they can also be observed on plants with hexagonal configurations, as in Fig. 6(a). Also note that one wavevector is preserved in each transition of the sequence (14). If one draws the curves

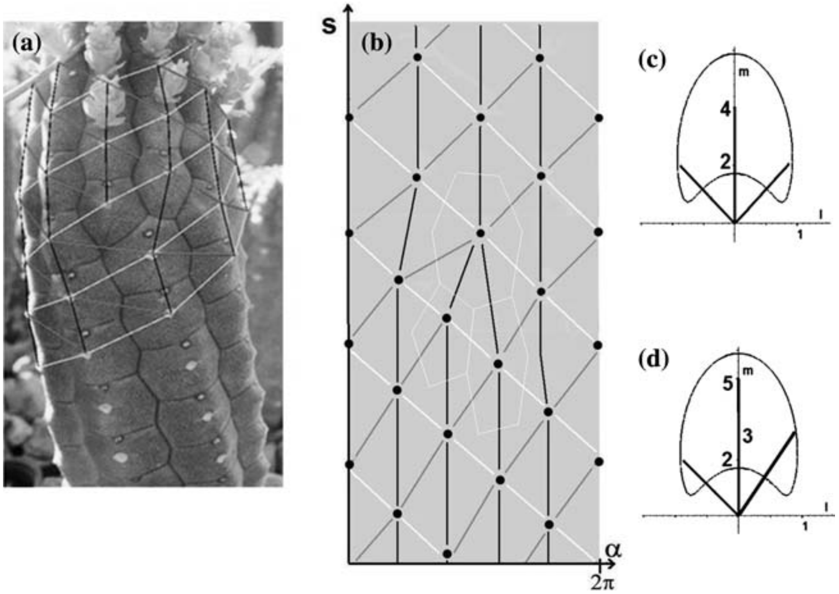

Fig. 6. (a) On a plant that undergoes a Type I transition one observes two dislocations (black and grey lines) and a family of spirals (white lines) that has no defect. (b) A Type I transition from a (2,2,4) alternating 2-whorl phyllotaxis (large values of s) to (2,3,5)-spiral phyllotaxis (small s) is drawn schematically. One spiral family (white lines) does not change during the transition. A penta-hepta pair is formed where the two dislocations in the other spiral families meet. The corresponding wavevectors are illustrated in (c) and (d) along with the typical boundary of the set of active modes. Reprinted from *Journal of Theoretical Biology*, P. D. Shipman and A. C. Newell, Polygonal Planforms and Phyllotaxis, accepted for publication 2005, with permission from Elsevier.

joining the maxima of the surface deformation in adjoining regions with different patterns, one sees dislocations in two families of spirals, corresponding to the two wavevectors that changed, and a penta-hepta defect at the point where the two dislocations meet. In Fig. 6, we illustrate this in the (s, α)-plane, with the transition between the phyllotactic lattices of the alternating 2-whorl (2,2,4) and (2,3,5)-spiral patterns.

4.2.3. Four-mode Configurations; Parallelogram Planforms

We have found that the most unstable triad is of the form $\vec{k}_m = (l, m), \vec{k}_n = (-l, n), \vec{k}_{m+n} = (0, m+n)$, where $m \simeq n$. The energy (7) allows for the interaction of multiple triads, and particularly for larger values of P there may be other triads in the active set that overlap with the optimal

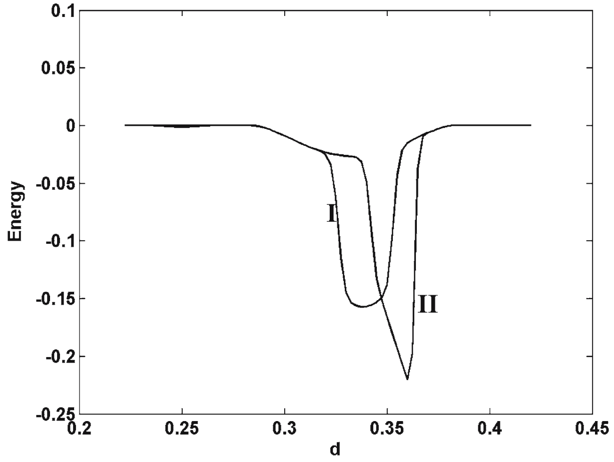

Fig. 7. For the choice of parameters $P = 2.4, \chi = 0, C = 3$, the energy (7) restricted to the sets of modes $\vec{k}_1 = (\frac{2\pi}{\lambda}(0 - 1d), m = 1), \vec{k}_2 = (\frac{2\pi}{\lambda}(1 - 2d), n = 2), \vec{k}_{m+n=3} = \vec{k}_1 + \vec{k}_2$ and either $\vec{k}_{2m+n=4}$ (curve I) or $\vec{k}_{m+2n=5}$ (curve II) was numerically calculated as a function of d and λ, and graphed is the lowest possible energy as a function of d.

triad. In particular, the wavevectors $\vec{k}_{2m+n} = \vec{k}_m + \vec{k}_{m+n}$ or $\vec{k}_{m+2n} = \vec{k}_n + \vec{k}_{m+n}$ may come into play. For $m = n$, $2m + n = m + 2n$, but if $n = m + 1$, the wavevectors $\vec{k}_{2m+n}$ and $\vec{k}_{m+2n}$ may not play symmetric roles; which mode is more likely to have a nonzero amplitude in an energy-minimizing configuration? The simplest way to check is to minimize the energy (7) restricted to the four modes with wavevectors $\vec{k}_m = (\frac{2\pi}{\lambda}, (q - md), m), \vec{k}_n = (\frac{2\pi}{\lambda}(p - nd), n), \vec{k}_{m+n} = \vec{k}_m + \vec{k}_n$ and either $\vec{k}_{2m+n} = \vec{k}_m + \vec{k}_{m+n}$ or $\vec{k}_{m+2n} = \vec{k}_n + \vec{k}_{m+n}$. The energy thus becomes a function of d and λ and our task is to find the energy-minimizing choices these parameters and the mode amplitudes for each choice of a fourth wavevector. Using our experience from the simple case of a single triad and the energy-minimizing choices $m \simeq n \simeq \frac{\Gamma}{2}$, consider the triads $\vec{k}_m, \vec{k}_{m+n}, \vec{k}_{2m+n}$ and $\vec{k}_m, \vec{k}_n, \vec{k}_{m+2n}$. The ratios $\frac{m,n}{m+2n}$ are closer to $\frac{1}{2}$ than are the ratios $\frac{m,n}{2m+n}$. For the choices $m = 1, n = 2$, for example, the ratios $\frac{1}{4}$ and $\frac{3}{4}$ are farther from $\frac{1}{2}$ than are the ratios $\frac{2}{5}$ and $\frac{3}{5}$. Although we do not have an analytic proof that this leads to a lower energy configuration with the wavevector choice $\vec{k}_{m+2n}$, it is confirmed by numerical experiments that this mode is energetically preferred. Fig. 7 demonstrates the energy (7) restricted to the sets of four modes with $m = 1, n = 2$ and either $\vec{k}_{2m+n=4}$ (curve I) or $\vec{k}_{m+2n=5}$ (curve II) as a function of d; the lowest energy is achieved for the latter wavevector choice at a value of $d \simeq 0.37$. (To produce the graph, we compute numerically, for values of d and λ in a reasonable range, the energy-minimizing amplitudes and the value of the energy (7); the graph shows, for each value of d, the lowest energy as a function of λ.) Note that this value of d is not exactly a value that makes any of the radial wavenumbers equal to 0; the energy-minimizing choice of d is possibly irrational. Due to the independence of the energies (5) and (7), after scaling, on Γ, similar results hold for larger values of m, n. In this case, the energy-minimizing amplitudes are such that $a_m \simeq a_{m+2n} < a_n \simeq a_{m+n}$; this produces parallelogram patterns with parastichy pair m, n; see Section 4.2.4.

4.2.4. Five Modes and Bias

Rather than separately testing the sets of overlapping triads $\vec{k}_m, \vec{k}_n, \vec{k}_{m+n}, \vec{k}_{2m+n}$ and $\vec{k}_m, \vec{k}_n, \vec{k}_{m+2n}$, we may allow for all five modes to compete together. That is, we restrict the energy (7) to the five modes $\vec{k}_m = (\frac{2\pi}{\lambda}, (q - md), m), \vec{k}_n = (\frac{2\pi}{\lambda}(p - nd), n), \vec{k}_{m+n} = \vec{k}_m + \vec{k}_n, \vec{k}_{2m+n} = \vec{k}_m + \vec{k}_{m+n}, \vec{k}_{m+2n} = \vec{k}_m + \vec{k}_{m+n}$, and find the energy-minimizing choices of λ, d and mode amplitudes. In Fig. 8(a) we show (curve I) the graph of the energy as a function of d for the choice $m = 2, n = 3, \Gamma = m + n = 5$. In this case, the energy reaches a local minimum at the choices $d \simeq 0.388$ (for which choice the amplitude A_7 is small and $A_2 \simeq A_8 < A_3 \simeq A_8$) and $d \simeq 0.412$ (for which choice the amplitude A_8 is small and $A_2 \simeq A_7 < A_3 \simeq A_5$). The latter choice is slightly lower, so that a parastichy pair (5,7) minimizes the energy.

This calculation, however, disregards the effects of a previous configuration that has formed for a smaller value of Γ and moved radially outward from the generative region. The effect of having, as a boundary condition, a previously produced configuration is to add constant terms c_j to the amplitude equations so that the evolution of the amplitudes is given by $\partial_t A_j = -\frac{\delta \mathfrak{E}'}{\delta A_j^*}$, where $\mathfrak{E}' = c_j A_j +$ complex conjugate $+ \mathfrak{E}$. Redoing the calculation of Fig. 8(a), curve I, but adding constant terms $c_2 = c_3 = c_5, c_7 = 0 = c_8$ to refect the chosen amplitudes for smaller Γ, the energy as a function of d is as shown in Fig. 8(a), curve II. In this case, it is the amplitude configuration $A_2 \simeq A_8 < A_3 \simeq A_5, A_7 \simeq 0$ and $d \simeq 0.378$ that are favored. Now increasing Γ in steps of 0.25 and using, as the constants c_j, the energy-minimizing choices of amplitudes from the previous value of Γ, the choice $d \simeq 0.378$ and the parastichy pair $(5, 8)$ remain preferred (Fig. 8(b)). Thus, the bias of a previous configuration helps to give preference to a parallelogram configuration with modes $\vec{k}_m, \vec{k}_n, \vec{k}_{m+n}, \vec{k}_{m+2n}$.

In these five-mode experiments, one mode, either that with wavevector $\vec{k}_{2m+n}$ or $\vec{k}_{m+2n}$ had a very small amplitude so that the energy-minimizing configuration was close to the solution of a four-mode competition

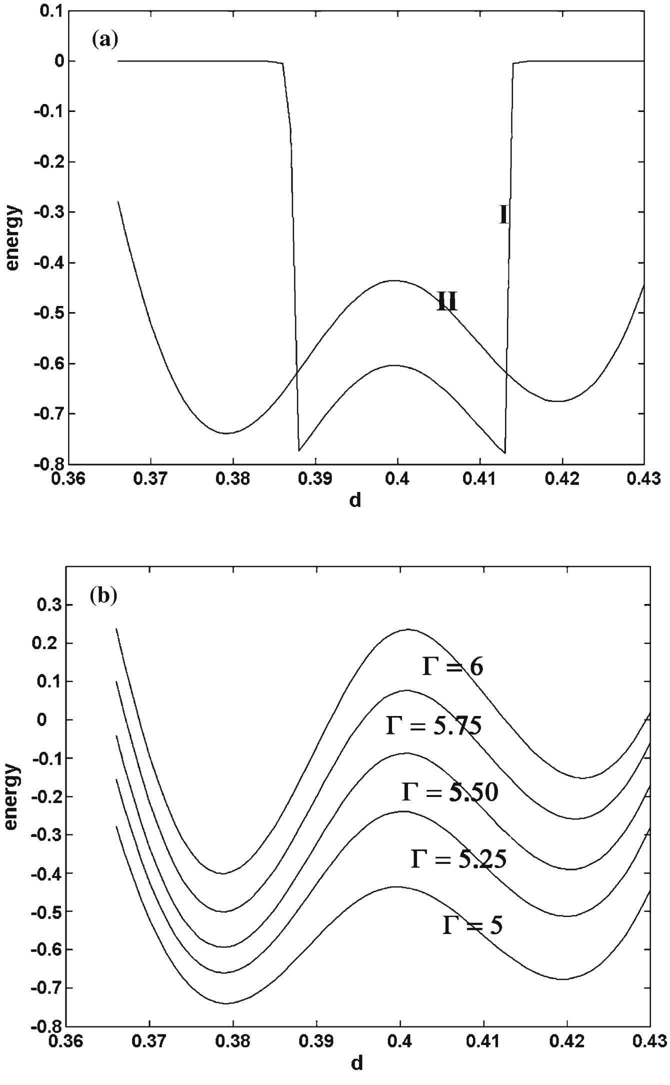

Fig. 8. For the choice of parameters $P=2.4$, $\chi=0, C=3$, the averaged energy $\mathfrak{E}$ restricted to the modes $\vec{k}_2=(\frac{2\pi}{\lambda},(1-2d),2), \vec{k}_3=(\frac{2\pi}{\lambda}(1-3d),3), \vec{k}_5=\vec{k}_2+\vec{k}_3, \vec{k}_7=\vec{k}_2+\vec{k}_5, \vec{k}_8=\vec{k}_3+\vec{k}_5$ becomes a function of d, λ and the amplitudes A_n of the modes for any given value of Γ. (a) For $\Gamma=5$ we calculated the energy-minimizing values of d, λ, A_n, and shown in curve I is the energy as a function of d. Curve II is the energy as a function of d for constant terms $c_2=c_3=c_5=0.5, c_7=c_8=0$ in the energy $\mathfrak{E}'$. (b) For increasing Γ, the energy $\mathfrak{E}$ is graphed as a function of d for increasing values of Γ. For each choice of Γ, the amplitudes of the previous choice of Γ were used as bias terms c_j in the energy $\mathfrak{E}'$.

with that mode absent. As a final example of a simplification of the energy (7), we again study a competition of five modes, but this time the five modes $\vec{k}_m, \vec{k}_n, \vec{k}_{m+n}, \vec{k}_{m+2n}, \vec{k}_{2m+3n}$. The energy-minimizing choice of d and the amplitudes are shown as functions of Γ in Fig. 9(a,b) for the choices $m=3, n=5$. No bias was added in this simple example. Notice that, as Γ increases, the amplitudes of the modes with smaller (respectively, larger) angular wavenumbers decrease (respectively, increase). For small Γ, the amplitude of the fifth mode (21) is negligible, and a parallelogram configuration like that of Section 4.2.3 is produced; see Fig. 9(a). For $\Gamma \simeq 12$, all five modes have significant amplitudes (although the outermost modes (3,21) are small). This produces a staircase parallelogram configuration; see Fig. 9(b). As Γ further increases, the amplitude of the mode with

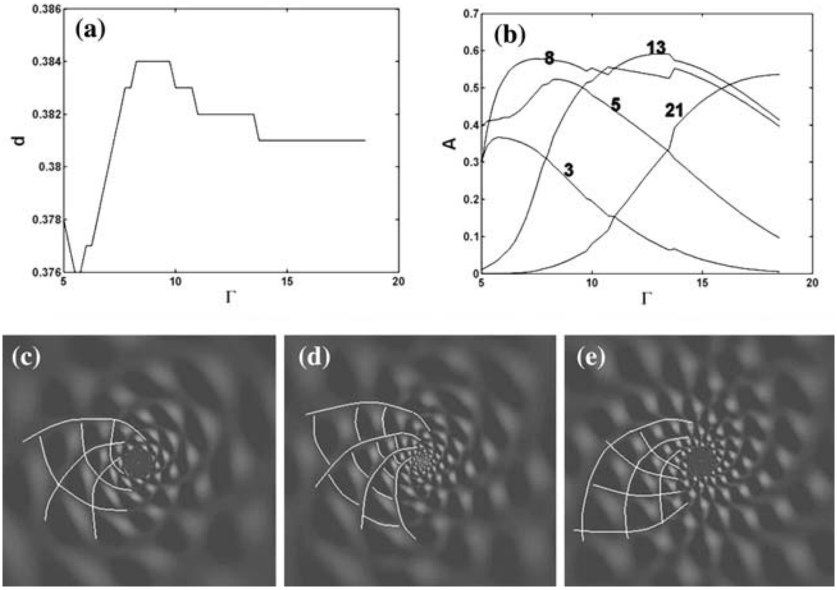

Fig. 9. For the parameters $C=3$, $\chi=0$, $P=2.7$ and modes with angular wavenumbers 3,5,8,13,21, we calculated (a) The energy-minimizing value of d as a function of Γ in the range $\Gamma=5,\ldots,18$. (b) The amplitudes of the 3,5,8,13,21 modes in the energy-minimizing configuration as Γ increases. (c–e) Deformations $w=a_3\cos(\vec{k}_3\cdot x)+a_5\cos(\vec{k}_5\cdot x)+a_8\cos(\vec{k}_8\cdot x)+a_{13}\cos(\vec{k}_{13}\cdot x)+a_{21}\cos(\vec{k}_{21}\cdot\vec{x})$, where $\vec{x}=(s=\ln(r),\alpha)$ and for values of d and the amplitudes a_j as determined by the experiment of (a,b), (c) at $\Gamma=8$, so that $d=0.383$, $a_3=0.3, a_5=0.52, a_8=0.58, a_{13}=0.3, a_5=0$, (d) at $\Gamma=11$, so that $d=0.3815$, $a_3=0.15, a_5=0.42, a_8=0.53, a_{13}=0.53, a_{21}=0.15$, and (e) at $\Gamma=14$, so that $d=0.3815$, $a_3=0.05, a+5=0.32, a_8=0.54, a_{13}=0.55, a_{21}=0.38$. Reprinted from *Journal of Theoretical Biology*, P. D. Shipman and A. C. Newell, Polygonal Planforms and Phyllotaxis, accepted for publication 2005, with permission from Elsevier.

angular wavenumber 3 decreases to zero and the planform is again that of parallelograms (Fig. 9(e)). Thus, a continuous transition from one parallelogram planform to another is achieved through a continuous change in amplitudes and divergence angle.

4.2.5. Type I or II Transitions

We have, for simplicity, separately considered the cases of 3,4, or 5 modes. To unite these ideas and give reasons for the choice of Type I or II transitions, we suggest the following picture: Imagine that, for the choice $\Gamma = m+n$, a sum of modes with amplitudes $\ldots, a_{m-n}, a_m, a_n, a_{m+n}, a_{m+2n}, \ldots$ is the energy-minimizing configuration. The configuration may consist of more modes, but the central modes are of largest amplitude as the growth rate of a mode with radial wavenumber j decreases for j further from $m+n$. The relative size of the amplitudes is determined by the parameters P and C. For small P, the linear growth rates, and therefore the amplitudes, of the outer modes, will be small (negligible), so that the configuration will be essentially that of a hexagon configuration $(m, n, m+n)$. For large (but not too large) P, the outer amplitudes are no longer negligible, and the configuration is that of parallelograms or staircase parallelograms. Similarly, a larger $|C|$ yields a larger interaction between modes with angular wavenumbers $(m-n, m, n)$ and thus increases the amplitude of the outer mode $m-n$ even if it is relatively strongly linearly damped.

Now suppose that the configuration $\ldots, a_{m-n}, a_m, a_n, a_{m+n}, a_{m+2n}, \ldots$, formed for $\Gamma \simeq m+n$, moves to the outer edge of the generative region and acts as a bias on a newly forming configuration. If Γ does not change, then the new configuration will be as the old one. However, if Γ increases, say to $m+n+1$, then the linear growth rate of the $m+2n$-mode increases, as does the linear growth rate of the mode $m+n+1$.

I. The true energy-minimizing configuration involves the optimal triad with radial wavenumbers $(m, n+1, m+n+1)$ and a Type I transition from the $(m, n, m+n)$ configuration.
II. However, if the amplitude a_{m+2n} is large in the bias configuration, it can grow continuously with Γ and give preference to a Type II transition in which the amplitudes a_{m+n} and a_{m+2n} grow continuously as the amplitudes a_{m-n}, a_n decay.

Thus, Type II transitions are more likely when the outer members of a sequence of amplitudes are larger. As a consequence, the theory predicts that ridge-dominated planforms are more likely to undergo Type I transitions, whereas parallelogram planforms are more likely to undergo Type II transitions. In agreement with the results of DC, the pattern produced by Type II transitions are not necessarily absolute energy minimizers, but rather local minimizers that are easily accessed from the previous configuration. It is important therefore to not only find energy-minimizing configurations, but also to understand how they can be accessed from the previous state.

5. DISCUSSION

We now return to the question posed in the introduction, namely

(i) Can the same theory describe ridge-shaped and polygonal planforms?
(ii) In the case of polygonal planforms, what determines the positions at which primordia (the polygons) form near the plant tip and therefore the phyllotactic pattern that develops?
(iii) What determines the type of phyllo that a primordium will develop into?

The first question is not addressed by DC, who assume that primordia of a given size and circular shape form on a parabaloid. Thus, in the DC model, the only difference in shape is the azimuthal elongation of primordia as determined by the conicity parameter N. Our model allows for all the commonly seen simple planforms and also suggests that there is a connection between ridge or hexagon patterns and Type I transitions and parallelogram patterns and Type II transitions–Type II transitions are more likely when there is more than one triad with significantly large amplitudes. Furthermore, the DC experiments suggest that the decussate (alternating 2-whorl) pattern can only be produced with azimuthally elongated primordia or conical apices and short-range interaction. Our model also produces ridge-dominated decussate patterns with radially elongated primordia as seen in some cacti.

To address the second question, which was the focus of the DC model, we first compare the parameters that were essential to both models. The main geometric parameter in the DC model is the ratio $\tilde{\Gamma} = \frac{d_0}{R}$ of the diameter of a newly formed primordium to the radius of the generative circle. This parameter has almost an exact analog in our model, namely the parameter Γ giving the ratio of the circumference of the central circle of the annular generative region to the natural wavelength; Γ is analogous to the inverse of $\tilde{\Gamma}$. Higher order phyllotactic patterns are produced as Γ (respectively, $\tilde{\Gamma}$) is increased (respectively, decreased).

The second geometric parameter concerns the curvature of the apex; DC define a conicity parameter N which determines the curvature of the apex. Our curvature parameter C is different in that it is only relevant in the generative region. In order to produce hexagon patterns in which the centers of the hexagons are the maxima (rather than the minima) of the deformation, our model requires that the geometry of the generative region be that of an inverted circle or hyperbolic, as depicted in Fig. 4(b,c). Our parameter C is also analogous to the DC stiffness parameter α. While α measures the degree that old primordia influences new ones (and thus a sort of interaction between primordia), in our model C measures the degree of interaction between triads of modes in the generative region. The essential difference between our two models is that primordia interact in the DC paradigm, whereas the elementary components that interact in our model are periodic modes.

DC propose, based on their paradigm, that the essential components for a mechanical model are that it (i) defines a finite area for new primordia, and (ii) allows for "repulsion" of some sort. Our mechanism does define a finite area $A = 2\pi\frac{\lambda}{g}R\Lambda$ which is essential for the results, but, instead of a repulsion between primordia, the essential points are that (1) the critical mode has wavevector $(0, \Gamma)$, (2) the interaction coefficient τ is sensitive to d and dependent on λ, (3) bias, which is relevant if there is one than one triad present, is essential to producing Type II transitions and the Fibonacci sequence. However, even if there is bias, if the deformation is dominated by one mode, Type I transitions are preferred over Type II transitions.

Regarding the difference between Type I and II transitions, DC propose that Type I transitions are preferred unless a quick change in Γ allows a continuous Type II transition to take hold. In our model, the Type I transition is also energetically preferred unless the deformation consists of more than one overlapping triad and a bias allows a mode of small amplitude to continuously grow in size with Γ. A consequence of this is the prediction that ridge-dominated planforms are more likely to undergo Type I transitions, whereas parallelogram planforms are more likely to undergo Type II transitions. While this conclusion conforms with our observations of cacti, there are no published data for a wide variety of plants. Green *et al.*(11) proposed that the difference between the formation of whorls and spirals (and thus, presumably between Type I and II transitions) is based on the width of the annular generative region. This is not included in our model, as we have approximated the Laplacian by the Euclidean Laplacian $\partial_r^2 + \frac{1}{\Gamma^2}\partial_\alpha^2$; a further modification of our model could test the idea of Green.

The DC model produces periodic (in d) transients during transitions between a (1,2,3) spiral and a decussate (2,2,4) phyllotactic pattern. Our model as presented here produces a sudden transition in which one

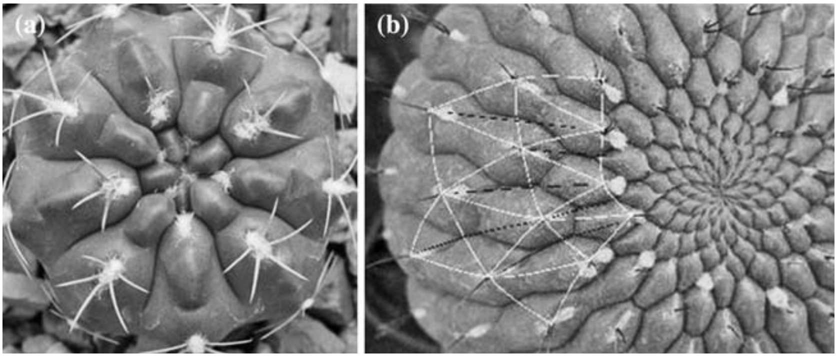

Fig. 10. (a) The hexagons on this cactus give way to ridges as they move from the plant tip, and (b) the parallelograms on this cactus give way to first hexagons and then rides as they move away from the plant tip. The hexagonal region determines three families of spirals, marked in white and corresponding to periodic deformations with wavevectors $\vec{k}_1, \vec{k}_2, \vec{k}_3 = \vec{k}_1 + \vec{k}_2$. The stickers, however, follow the spirals, marked in black, corresponding to the wavevector $\vec{k}_4 = \vec{k}_2 + \vec{k}_3$.

wavevector is preserved. Both transition types are seen in nature; adding spatial derivative terms to our model should be able to test if and under what conditions periodic transients can occur.

We now turn to the third question. Our fifth hypothesis in Section 3.2 states that, outside of a region R, there is not further change in the deformation w except that the amplitudes may grow uniformly. On a typical plant, however, the primordium will eventually develop into a mature phyllo–a leaf, a floret or any of many other intricate structures. Fig. 10 shows simple cases of the change in deformations w as they move away from the apex. In Fig. 10(a), one observes that a hexagon pattern can change into a ridge pattern as the material matures; the purely circumferential mode grows in amplitude faster than the other two modes in the triad. In Fig. 10(b), a parallelogram planform first changes into a hexagonal planform and then a ridge-dominated planform as the material matures. The phyllotactic pattern—the lattice of the deformation's maxima—does not change, but the relative sizes of the amplitudes may change as the material moves away from the apex. These simple examples of how primordia may mature indicate that, at least in some cases, the different modes of a plant's configuration are amplified to different degrees. It may be that a slight dominance of a purely radial deformation at the plant tip may induce changes in cell division and cellulose orientation (microscopic responses to macroscopic buckling, as proposed by Green *et al.*[(11)]) or a nonuniform hormone distribution in response to changes in stress.

Furthermore, note in Fig. 10(b) that, even as one spiral mode (marked in black) decays in amplitude, the stickers that form are aligned along the direction of this decaying mode. Thus, although the processes that lead to intricate phylla such as leaves or florets are much more involved than these simple examples, the presence of elementary modes suggest simple ways in which to study the feedback mechanisms between stresses, chemistry and growth.

In contrast to the suggestion made above that mechanical buckling initiates primordia and is followed by changes in plant hormone concentrations, a growing biological community believes that the initiation of primordia is also chemical. In particular, recent work has focused on the growth hormone auxin and the role of the PIN1 protein in auxin transport; see Reinhardt,(14) for a review. Models based on these ideas are able to reproduce spiral or whorl patterns, but, like the DC model, do not explain ridge patterns.

In,(16) we further discuss predictions of the mechanical model and suggest experiments and observations to test the theory.

REFERENCES

1. T. M. Atanackovic and A. Guran, *Theory of Elasticity for Scientists and Engineers* (Birkhaeuser, 2000).
2. S. Douady and Y. Couder, phyllotaxis as a physical self-organizing growth process, *Phys. Rev. Lett.* **68**:2098–2101 (1992).
3. S. Douady and Y. Couder, Phyllotaxis as a dynamical self-Organizing process, part i: The spiral modes resulting from time-periodic iterations, *J. Theor. Biol.* **178:**255–274 (1996).
4. S. Douady and Y. Couder, Phyllotaxis as a dynamical self-organizing process, part ii: The spontaneous formation of a periodicity and the coexistance of spiral and whorled patterns, *J. Theor. Biol.* **178**:275–294 (1996).
5. J. Dumais and C. R. Steele, New Evidence for the role of mechanical forces in the shoot apical meristem, *J. Plant Growth Reg.* **19**:7–18 (2000).
6. J. Färber, H. C. Lichtenberger, A. Reiterer, S. Stanzl-Tschegg, and P. Fratzl, Cellulose microfibril angles in a spruce branch and mechanical implications, *J. Mat. Sci.* **36**:5087–5092 (2001).
7. A. J. Fleming, S. McQueen-Mason, T. Mandel, and C. Kuhlemeier, Induction of Leaf Primordia by the Cell Wall Protein Expansin, Science **276**:1415–1418 (1997).
8. P. L. Gould, Analysis of Plates and Shells, (Prentice Hall, 1999).
9. P. Green, Expression of Pattern in Plants: Combining Molecular and Calculus-Based Biophysical Paradigms, *Am. J. Bot.* **86**:1059–1076 (1999).
10. P. B. Green, Expression of form and pattern in plants. a role for biophysical fields, *Cell. Dev. Biol.* **7**:903–911 (1996).
11. P. B. Green, C. S. Steele, and S. C. Rennich, How plants produce patterns. A review and a proposal that undulating field behavior is the mechanism, in *Symmetry in Plants*, Roger V. Jean and Denis Barabé, eds. (World Scientific, 1998).
12. L. H. Hernández and P. B. Green, Transductions for the Expression of Structural Pattern: Analysis in Sunflower, *Plant Cell* **5**:1725-1738 (1993).

13. W. Hofmeister, *Allgemeine Morphologie der Gewachse, Handbuch der Physiologischen Botanik*, (Engelmann, 1868).
14. D. Reinhardt, A new chapter in an old tale about beauty and magic numbers, *Current Opinion in Plant Biology* **8**:1–7 (2005).
15. P. D. Shipman and A. C. Newell, Phyllotactic patterns on plants, *Phys. Rev. Lett*. **92**:168102 (2004).
16. P. D. Shipman and A. C. Newell, polygonal planforms and phyllotaxis on plants, *J. Theo. Biol*. **236**:154–197 (2005).
17. M. Snow and R. Snow, Minimum areas and leaf determination, *Proc. Roy. Soc*. 545–566 (1952).
18. C. R. Steele, Shell stability related to pattern formation in plants, *J. Appl. Mech*. **67**:237–247 (2000).
19. H. Yamamoto, generation mechanism of growth stresses in wood cell walls, *Wood Sci. and Technol*. **32**:171–182 (1998).